A theoretical description and experimental demonstration of diffraction in electron-stimulated desorption

2010 J. Phys.: Condens. Matter 22 084001

(http://iopscience.iop.org/0953-8984/22/8/084001)

J. Phys.: Condens. Matter **22** (2010) 084001 (11pp) doi:10.1088/0953-8984/22/8/084001

A theoretical description and experimental demonstration of diffraction in electron-stimulated desorption

Doogie Oh[1], Matthew T Sieger[2] and Thomas M Orlando[1,3,4]

[1] School of Chemistry and Biochemistry, Georgia Institute of Technology, Atlanta, GA 30332, USA
[2] Effiscience, Knoxville, TN 37923, USA
[3] School of Physics, Georgia Institute of Technology, Atlanta, GA 30332, USA

E-mail: Thomas.Orlando@chemistry.gatech.edu

Received 21 September 2009
Published 4 February 2010
Online at stacks.iop.org/JPhysCM/22/084001

Abstract

The role of diffraction in electron-stimulated desorption (DESD) is demonstrated experimentally and described theoretically. Specifically, initial state effects in DESD of Cl^+ from Si(111)-(1 × 1):Cl and Si(111)-(7 × 7):Cl are examined and a theoretical treatment that includes spherical-wave effects and multiple scattering of low-energy incident electrons is presented. Although contributions from complicated defect configurations such as $SiCl_2$ and $SiCl_3$ cannot be ruled out, comparison of the experimental data with theory indicates that Cl^+ desorption from Si(111)-(1 × 1):Cl and Si(111)-(7 × 7):Cl surfaces may be dominated by monochloride terminal sites. The initial states probably contain significant Si 3s and/or Si–Cl σ-bonding character. In the Si(111)-(7 × 7):Cl case, these excitations favor a propensity for Cl^+ desorption from the unfaulted, rather than faulted, zones of the 7 × 7 reconstructed rest atom area. This propensity may be related to increased screening and hole localization in the Si–Si backbonds within the faulted region. Finally, introducing Debye–Waller factors into each scattering path accounts for much of the experimentally observed DESD width broadening at room temperature.

(Some figures in this article are in colour only in the electronic version)

1. Introduction

Low-energy (<100 eV) electrons are used to examine surface electronic and atomic structure and are often the probe of choice due to their small penetration depth and strong interaction with the solid. Incident low-energy electron beams have been used for popular surface analysis techniques such as low-energy electron diffraction (LEED) and variants thereof. Other techniques, such as electron energy loss spectroscopy (EELS), secondary electron emission (SEE), Auger electron spectroscopy (AES), and inverse photoemission (IP) depend upon the transfer of energy from the incident electron beam to the solid by an inelastic scattering event. For adsorbate covered surfaces and condensed phase targets, the inelastic channels can be collective, multi-electron excitations that often 'localize' in an adsorbate-substrate or surface complex [1–6]. When this type of localization of electronic energy occurs, non-thermal desorption can ensue via a process known as desorption induced by electronic transitions (DIET). If DIET is initiated by electrons, the overall process is simply referred to as electron-stimulated desorption (ESD) [6]. A very useful technique known as electron-stimulated desorption ion angular distributions (ESDIAD) has been developed to probe the bonding sites of a wide variety of adsorbate covered surfaces [6, 7]. ESDIAD has been used to show the bonding geometry of Cl atoms on the Si(100)-(2 × 1) surface [8]. For the study of Cl^+ desorption from Si surfaces, ESD has been used and useful information including the threshold energy has been gleaned [9–12].

Previously, we observed interference effects in the electron-stimulated desorption of Cl^+ from Cl terminated

[4] Author to whom any correspondence should be addressed.

Si(111) surfaces and referred to this potentially useful effect as diffraction in electron-stimulated desorption (DESD) [13, 14]. Related work on standing wave effects in high-energy (e.g. >1 keV x-rays) photon-stimulated desorption (XPSD) of ions from semiconductor surfaces has also been reported [15–17]. Analysis of the x-ray standing wave (XSW) difference spectra obtained at the Cl 1s absorption edge allowed identification of the ESD active sites from the Si(111)-(1 × 1):Cl surface and separation of the direct and indirect contributions to ion desorption [15]. A recent analysis of the XSW and XPSD data in conjunction with density functional modeling of the Si(111):Cl system suggests that $SiCl_3$ terminal sites maybe selectively revealed [17]. Since DESD relies upon initial state effects and utilizes lower-energy (<50 eV) electrons with low penetration depths, site specific desorption should also be observable especially near threshold.

In this paper, we re-examine the DESD of Cl^+ from Si(111)-(1 × 1):Cl [13, 14] and present information on the Si(111)-(7 × 7):Cl surfaces that demonstrates the ability to extract site specific desorption information. We also describe DESD with an abridged theoretical description based, in part, upon previous LEED [18], extended x-ray absorption near edge structure (XANES) [19], and photoelectron diffraction [20] theories. The generalized DESD theory and results of example calculations are presented in sections 2 and 3, respectively. Section 4 contains the experimental results, and a comparison to theory. A discussion of the plausible desorption mechanism(s) is given in section 5. Finally, conclusions and a short discussion of the potential utility of this approach are given in section 6.

2. Theory

The rate for ESD can be represented by the product of the electronic excitation cross section and the desorption probability according to the Menzel–Gomer–Redhead (MGR) model [4] in which desorption occurs due to the repulsive excited state potential. For ion desorption from ionic or covalent surfaces, Knotek and Feibelman proposed a model involving direct ionization followed by Auger decay [5]. To date, most theoretical treatments have concentrated on final state effects [21–23]. Essentially no theoretical treatments have focused on the potential importance of initial state effects such as diffraction and interference. In this paper, we present the most relevant details of a useful mathematical description of how diffraction can influence ESD. We begin with Fermi's golden rule to derive the ESD rate according to the theory of impact ionization (e–2e) spectroscopy of solids [24–26]. This approach can be justified because the ESD desorption rate is proportional to the excitation rate.

We use Hartree atomic units, $e = \hbar = m = 1$ for all mathematical expressions. By Fermi's golden rule, the excitation rate in ESD is expressed as

$$\Gamma_{\mathrm{i}\to\mathrm{f}} = 2\pi\,|\langle 34|H_{\mathrm{ee}}|12\rangle|^2 \rho_{\mathrm{if}}\delta(E_{\mathrm{f}} - E_{\mathrm{i}}), \tag{1}$$

where ρ_{if} is the density of the initial and final states, H_{ee} is the electron–electron interaction Hamiltonian, and the δ–function conserves the total system energy. The initial state of the projectile (target) electron is labeled by the index 1 (2), and the final state of the projectile (target) electron is labeled 3 (4). We assume ion desorption is initiated by a screened shallow or deep core level and do not treat final state effects. We ignore extended (valence) initial state target electron density. Also, the electron–electron interaction Hamiltonian can be expressed in a simple form which does not account for small magnetic and retardation effects in low-energy electron collisions. The final form without considering electron exchange is approximated by

$$\Gamma_{\mathrm{if}} \propto \int\int \rho_1(\mathbf{k},\mathbf{r})\frac{\mathrm{e}^{-2a|\mathbf{r}-\mathbf{r}'|}}{|\mathbf{r}-\mathbf{r}'|^2}\rho_2(\mathbf{r}')\,\mathrm{d}\mathbf{r}\,\mathrm{d}\mathbf{r}', \tag{2}$$

where $\rho_1(\mathbf{k},\mathbf{r})$ is the charge density of the incident electron with wavevector $\mathbf{k}$, $\rho_2(\mathbf{r}')$ the charge density of the target electron, and a screened Coulomb interaction represents the electron–electron interaction Hamiltonian with screening length a^{-1}. The screening length we used in these calculations is short so that the interaction integral can be reduced to the point overlap integral.

In order to calculate the interaction integral, we need to obtain the complete description of the incident electron density on the surface. The electron density is formed by the interference of the directly incoming electron wave with wave components elastically scattered by the near-surface atoms. Therefore, the incident electron wavefunction, $\phi(\mathbf{r})$ can be expanded in a multiple scattering series

$$\phi(\mathbf{r}) = \phi^0(\mathbf{r}) + \phi^1(\mathbf{r}) + \phi^2(\mathbf{r}) + \cdots + \phi^N(\mathbf{r}), \tag{3}$$

where successive terms represent no scattering, single scattering, double scattering, etc. In the limit, as $N \to \infty$, ϕ represents the solution to the time-independent Schrödinger equation in the solid. In the limit as $\mathbf{r} \to \infty$ this formalism reduces to LEED theory.

We assume that the ESD rate is proportional to the probability of finding the incident electron in the vicinity of the absorber located at $\mathbf{R}_{\mathrm{a}}$, or $I \propto \phi^*(\mathbf{R}_{\mathrm{a}})\phi(\mathbf{R}_{\mathrm{a}})$, where $\phi(\mathbf{r})$ is the electron wavefunction in the presence of the surface. In the absence of scattering, the incident electron wavefunction is

$$\phi^0(\mathbf{r}) = \langle\mathbf{r}|\mathbf{k}\rangle = \mathrm{e}^{\mathrm{i}\mathbf{k}\cdot\mathbf{r}}\mathrm{e}^{-z/\Lambda\cos(\theta)}, \tag{4}$$

where $\mathbf{k}$ is the electron wavevector, corrected for refraction through the inner potential V_0. The right-hand exponential represents attenuation of the incident plane wave from inelastic scattering processes, where the mean free path is Λ, z is the vertical distance traveled in the solid, and θ is the angle between $\mathbf{k}$ and the surface normal.

The electron wavefunction in the presence of the surface can be approximated to first order by

$$\phi(\mathbf{r}) \approx \phi^0(\mathbf{r}) + \sum_{i=1}^{N}\phi^0(\mathbf{R}_i)\,f(\theta_s)\frac{\mathrm{e}^{\mathrm{i}k|\mathbf{R}_i-\mathbf{r}|}}{k|\mathbf{R}_i-\mathbf{r}|}\mathrm{e}^{-|\mathbf{R}_i-\mathbf{r}|/\Lambda}, \tag{5}$$

where $\mathbf{R}_i$ are bond vectors of the N lattice atoms in the cluster surrounding the absorber at $\mathbf{R}_{\mathrm{a}}$. The scattering factor $f(\theta)$ is obtained by the usual asymptotic atomic scattering formula

$$f(\theta) = \sum_l (2l+1)\mathrm{e}^{\mathrm{i}\delta_l}\sin(\delta_l)P_l(\cos\theta), \tag{6}$$

where l is angular momentum quantum number, $e^{i\delta_\ell}\sin(\delta_l)$ is the scattering matrix, and $P_l(\cos\theta)$ is the Legendre polynomial. This model evokes several simplifying approximations: (1) spherical-wave effects are neglected, (2) the interaction with the absorber is assumed to occur at a point (point-excitation approximation) (3) the absorber potential is ignored, and (4) the effect of lattice vibrations is neglected. While admittedly simplified, this model is sufficient to reproduce the essential features of the relevant physics, and is valid in the limit of high electron energy ($E > \sim$1 keV) and short mean-free-paths.

At low electron energies (<1 keV) and short bond lengths ($kR < \sim$10), spherical-wave effects are important for low energy electrons and short scattering distances. We must account the curvature of the wavefront as opposed to using the simplifications offered by the plane wave treatment. In order to take into account the curved-wave effect and also to expand the formulae in a multiple scattering series for low-energy electron diffraction, several approaches have been introduced. Among them, path approaches based on the perturbation method were successfully used in extended x-ray absorption fine structure (EXAFS) and photoelectron diffraction (PED) [19] theories. Although they are not as exact as diagonalization methods, the short mean free path of the photoelectron makes them very competitive because long paths are smeared out by short lifetimes, and in the limit of full multiple scattering (all paths included) they approach the exact results.

In the path approach, an incoming electron is perturbed by components scattered through hypothetical paths. Each scattering path is generated by selecting some number of atoms inside the atomic cluster. Each perturbation component of an incident electron for each path is the product of the scattering t-matrix and Green's function for each atom summed over all atoms constituting a specific path. Equation (7) yields an exact expression

$$|\phi\rangle = (1 + GT)|\mathbf{k}\rangle, \tag{7}$$

where G and T are Green's function and the scattering T-matrix for the entire system. A common approach to solving this equation is given by the Dyson expansion and successive terms represent no scattering, single scattering, double scattering, etc [19]. The direct term (no scattering) reduces to the amplitude and phase of the incident plane wave at the absorber, and can be arbitrarily set to unity. To obtain an expression for the single scattering amplitude, we insert complete sets of states in the displaced spherical-wave basis

$$\langle \mathbf{r}|k, L; \mathbf{R}\rangle \equiv i^l j_l(k|\mathbf{r} - \mathbf{R}|)Y_l^m(\Omega_{\mathbf{r}-\mathbf{R}}). \tag{8}$$

Strictly, this functional form is valid only in the region of constant potential between muffin-tin spheres. The single scattering amplitude reduces to

$$\phi^1(\mathbf{r}) = \sqrt{4\pi}\sum_i \sum_L G_{0L}(\vec{\rho}_{\mathbf{r}i})t_l^i Y_L^*(\hat{\mathbf{k}})e^{i\mathbf{k}\cdot\mathbf{R}_i}, \tag{9}$$

where $\vec{\rho}_{\mathbf{r}i} = k(\mathbf{R}_a - \mathbf{R}_i)$, $\mathbf{R}_a$ being the absorber position and $\mathbf{R}_i$ is a lattice vector. It can be easily shown that the double scattering amplitude is

$$\phi^2(\mathbf{r}) = \sqrt{4\pi}\sum_{i,j\neq i}\sum_{L,L'} G_{0L}(\vec{\rho}_{\mathbf{r}j})t_l^j G_{LL'}(\vec{\rho}_{ji})t_{l'}^i Y_{L'}^*(\hat{\mathbf{k}})e^{i\mathbf{k}\cdot\mathbf{R}_i}. \tag{10}$$

What remains is to calculate the free-space Green's function propagator. To do this, we adopt Rehr and Albers' separable propagator method [19]. Green's function in this formalism is the free propagator, $G_{LL'}(\vec{\rho}) = \langle L, \mathbf{R}|G|L', \mathbf{R}'\rangle$ with $\vec{\rho} = k(\mathbf{R} - \mathbf{R}')$. This is defined as the coefficient in the expansion in the spherical wave of the dimensionless outgoing free propagator. $G_{LL'}(\vec{\rho})$ is expressed as

$$G_{LL'}(\vec{\rho}) = \frac{e^{i\rho}}{\rho}\sum_\lambda \tilde{\Gamma}_\lambda^L(\vec{\rho})\Gamma_\lambda^{L'}(\vec{\rho}), \tag{11}$$

where λ represents the matrix index (μ, ν). The procedure of deriving $\tilde{\Gamma}_\lambda^L(\vec{\rho})$ and $\Gamma_\lambda^{L'}(\vec{\rho})$ can be found in [19]. We just write the result.

$$\begin{aligned}\Gamma_\lambda^{L'}(\vec{\rho}) &= R^{l'}_{\mu m'}(\Omega_{\hat{\rho}})\gamma^{l'}_{\mu\nu}(\vec{\rho}),\\ \tilde{\Gamma}_\lambda^{L}(\vec{\rho}) &= R^{l}_{m\mu}(\Omega_{\hat{\rho}}^{-1})\tilde{\gamma}^{l}_{\mu\nu}(\vec{\rho}).\end{aligned} \tag{12}$$

As demonstrated for EXAFS and PED calculations, this form of the propagator is convenient for multiple scattering calculations because it is possible to separate waves expanded in L from those expanded in L'. We used the scattering matrices and explicit definitions given by Rehr and Albers [19]. The introduction matrix $\mathbf{P}_\lambda$ describes the direct collision of an incoming electron into one of the scatters in the near-surface region. The scattering matrix $\mathbf{F}_{\lambda\lambda'}$ represents intermediate steps that determine the scattering and the termination matrix $\mathbf{M}_\lambda$ is used to guide the scattered electron into the absorber. Calculations of LEED, EXAFS and PED utilize different introduction and termination matrices. The scattering matrix $\mathbf{F}_{\lambda\lambda'}$ is the same as that defined for the multiple scattering treatment of EXAFS and PED [27]. The primary difference in our calculations describing DESD is in the treatment of the incoming wave and the detection point. The incident electron amplitude can be written concisely for any scattering order,

$$\phi^1(\mathbf{r}) = \sum_i\sum_\lambda \mathbf{M}_\lambda(\vec{\rho}_{\mathbf{r}i})\mathbf{P}_\lambda(\vec{\rho}_{\mathbf{r}i}, \hat{\mathbf{k}})\frac{e^{i\rho_{\mathbf{r}i}}}{\rho_{\mathbf{r}i}}e^{i\mathbf{k}\cdot\mathbf{R}_i} \tag{13}$$

$$\phi^2(\mathbf{r}) = \sum_{i,j\neq i}\sum_{\lambda,\lambda'} \mathbf{M}_\lambda(\vec{\rho}_{\mathbf{r}j})\mathbf{F}_{\lambda\lambda'}(\vec{\rho}_{\mathbf{r}j}, \vec{\rho}_{ji})\mathbf{P}_{\lambda'}(\vec{\rho}_{ji}, \hat{\mathbf{k}}) \times \frac{e^{i\rho_{\mathbf{r}j}}}{\rho_{\mathbf{r}j}}\frac{e^{i\rho_{ji}}}{\rho_{ji}}e^{i\mathbf{k}\cdot\mathbf{R}_i}. \tag{14}$$

If we compare these expressions to plane-wave formulae of equation (5), we see that the spherical-wave treatment can be condensed into calculating effective scattering amplitudes f_{eff} for each order of scattering;

$$f^1_{\text{eff}}(\vec{\rho}_{\mathbf{r}i}, \hat{\mathbf{k}}) = \sum_\lambda \mathbf{M}_\lambda(\vec{\rho}_{\mathbf{r}i})\mathbf{P}_\lambda(\vec{\rho}_{\mathbf{r}i}, \hat{\mathbf{k}}) \tag{15}$$

$$f^2_{\text{eff}}(\vec{\rho}_{\mathbf{r}j}, \vec{\rho}_{ji}, \hat{\mathbf{k}}) = \sum_{\lambda,\lambda'} \mathbf{M}_\lambda(\vec{\rho}_{\mathbf{r}i})\mathbf{F}_{\lambda\lambda'}(\vec{\rho}_{\mathbf{r}j}, \vec{\rho}_{ji})\mathbf{P}_{\lambda'}(\vec{\rho}_{ji}, \hat{\mathbf{k}}). \tag{16}$$

Figure 1 is a diagram of the scattering process in a sequential manner. Three scattering paths are shown in the near-surface region. They are the first-, second-, and third-order scattering components. The incident electron wavevector $\mathbf{k}'$ is refracted into $\mathbf{k}$ due to the inner potential V_0. This refracted wavefunction is phase-shifted when it first encounters

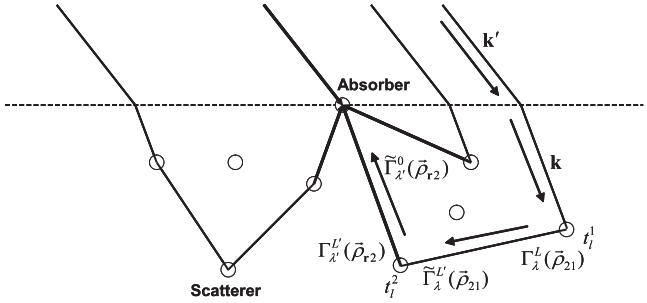

Figure 1. Three scattering paths in the near-surface region are shown. They represent the first-order, second-order, and third-order scattering components. The components scattered into the absorber interfere with the incoming electron beam and form local maxima or minima. For the second-order path, separable propagator terms are added to describe the scattering procedure illustratively. (i) The incident electron wavevector $\mathbf{k}'$ is refracted into $\mathbf{k}$ due to the inner potential V_0. (ii) This refracted wavefunction is phase-shifted by the scattering potential which is expressed by a scattering t-matrix, t_l^1. (iii) The electron then interacts with the second scattering center. Steps (ii) and (iii) are symbolized by an introduction matrix. The scattering event at the second atom is represented by a scattering matrix. Finally, a termination matrix is then introduced at the absorber site. Each scattering step matches the corresponding mathematical terms in the separable propagator expression sequentially. The scattering order can be easily expanded by multiplying additional scattering matrices along the path.

the scattering potential and is represented by multiplication of the scattering matrix t_l^1. The next step involves scattering of the electron into the second scatterer. Up to this point, the process is symbolized by the introduction matrix. The scattering procedure at the second atom is represented by a scattering matrix. Finally, the termination matrix is introduced at the absorber site. As you can see, the scattering procedure exactly follows the separable propagator expression with each scattering step matching the corresponding mathematical term sequentially. The scattering order can be easily expanded just by multiplying additional scattering matrices along the path. Note that components scattered into the absorber interfere with the direct electron beam and form local maxima or minima of incident electron intensity.

Finally, we have to add two more parts which take into account the inelastic scattering and thermal effects for each scattering path. The inelastic scattering term is the same as that used in the plane-wave approximation. Actually, it originates from the dimensionless outgoing free propagator (equation (11)) by replacing the real energy $\varepsilon + i0^+$ with the complex energy $\varepsilon + i\Lambda$. The temperature effect can be included by introducing the appropriate Debye–Waller factor. When these two terms are included into each scattering path, the first-order scattering amplitude becomes

$$\phi^1(\mathbf{r}) = \sum_i \sum_\lambda \mathbf{M}_\lambda(\vec{\rho}_{\mathbf{r}i})\mathbf{P}_\lambda(\vec{\rho}_{\mathbf{r}i}, \hat{\mathbf{k}})\mathrm{e}^{-|\frac{\vec{\rho}_{\mathbf{r}i}}{\hat{\mathbf{k}}}|/\Lambda} W_i(T)\frac{\mathrm{e}^{\mathrm{i}\rho_{\mathbf{r}i}}}{\rho_{\mathbf{r}i}}\mathrm{e}^{\mathrm{i}\mathbf{k}\cdot\mathbf{R}_i}. \tag{17}$$

We then use this to calculate $I \propto \phi^*(\mathbf{R}_\mathrm{a})\phi(\mathbf{R}_\mathrm{a})$ as a function of incident electron energy and $\mathbf{k}$-vector.

3. Calculations

3.1. The separable propagator method versus plane-wave approximation (PWA)

Although the description of incident electrons inside the absorber muffin-tin potential is important for DESD due to the presence of the absorber potential, it is skipped as part of the simplifying assumptions. The effect of the muffin-tin potential representing the atoms surrounding the absorber are accounted for in the partial-wave phase shifts computed for those potentials. These data are used to produce the scattering amplitude of the incident electron around a scattering potential and to calculate the incident electron density. Since the scattering amplitude can directly give us qualitative DESD results, we calculate scattering amplitudes using equation (6) for the plane-wave approximation and equation (15) for the separable propagator method. In the case of the separable propagator approach, only the lowest-order (1×1) matrix $\mathbf{F}_{\lambda\lambda'=(00,00)}$ is used to calculate the effective scattering amplitude. Other matrix elements with higher-order indices vanish because the termination matrix of each scattering path only allows for zero angular momentum. Partial-wave phase shifts for each atom were calculated with the FEFF 7.0 code developed by Rehr *et al* [28, 29].

In order to quantitatively compare this separable propagator method with the plane-wave approximation, the variable kR (i.e. the similarity of the scattering amplitude to that of the plane-wave approximation) is introduced. In the case of $kR = 2$, differences between the two methods are substantial. Although these are not shown, there are large amplitudes for forward scattering relative to other amplitudes and distinct features at 120° and 240°. As kR increases, the shape of the scattering amplitude becomes closer to that of the plane-wave approximation. Because the long scattering paths are smeared out by the inelastic scattering of the incident electron, the curved-wave effect turns out to be important in calculating the electron density at the absorber site.

In the calculation of DESD by the separable propagator method, computation time limits the calculation accuracy due to the long times needed for all scattering paths. Therefore, we approximate the calculation by using the plane-wave approximation in scattering paths involving kR larger than 50. In this regime, the calculated amplitudes of the separable propagator method are almost the same as that of the PWA.

3.2. Calculation of k-space projection profiles

In this section, we present and discuss the calculation using the electron-induced desorption of Cl^+ for the Si(111)-(1 × 1):Cl and Si(111)-)-(7 × 7):Cl surfaces. Specifically, we calculate the incoming electron density for the site of an absorber atom as a function of the electron $\mathbf{k}$-vector. In the Si(111)-(1 × 1) case, relaxation of the top Si layers was not taken into account. In the calculation of the Si(111)-(7 × 7):Cl, we explicitly treat the A and B terminations. Figure 2 shows the schematic structures of Si(111) surfaces. The original geometry for the Si(111)-(7 × 7) has been obtained from a database [30]. For simplicity, the Si(111)-(7 × 7)A:Cl surface is assumed to have only adatoms

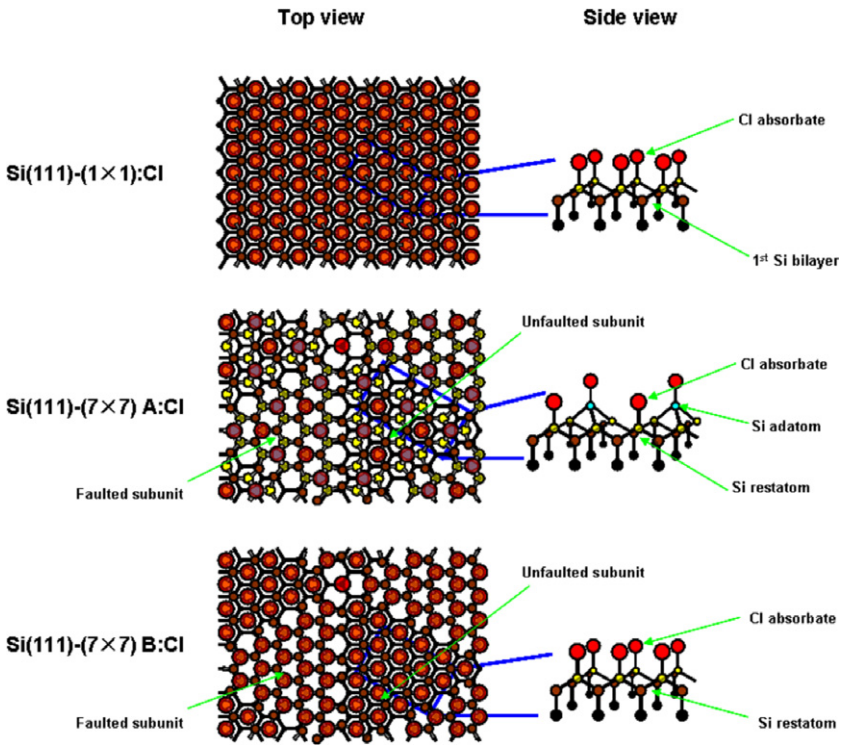

Figure 2. Si(111) surfaces which have been used for the calculations. The top part shows the Si(111)-(1 × 1):Cl structure. Gray (red online) circles correspond to Cl adsorbates which are directly bonded to Si atoms. The middle part shows the Si(111)-(7 × 7)A:Cl terminated surface. Each of the 6 Cl adsorbates in the unfaulted and the faulted subunits are gray (red online). One more Cl adsorbate is located on the corner hole. The bottom part shows the Si(111)-(7 × 7)B:Cl terminated surface. There are 42 Cl adsorbates shown as gray (red online) on each unit cell.

which are monochlorides even though the real surfaces may contain some di- or tri-chlorides. For the Si(111)-(7 × 7)B:Cl surface, it is assumed that all adatoms are stripped away and all rest atoms are bonded by Cl. As will be shown later, we have also defined several sites in the faulted and unfaulted region and these will be discussed further in section IV.D.

For the complete calculation, the atomic cluster size should be chosen to generate the whole scattering path. However, due to the short electron inelastic mean free path that smears the amplitude induced by long scattering paths, a reduced cluster diameter less than about 50 Å can be used. In our calculation, a hemispherical 'cluster' of 1028 atoms within 20 Å to an absorber was chosen. For the Si(111)-(1 × 1):Cl surface, the experimental Si–Cl bond length used is 2.03 Å [31] and the inner potential V_0, is assumed to be 16 eV. Most calculations described in this section have been done at 300 K. A brief discussion of temperature affects will be dealt with in section 5.2. The direction of the incident electron **k**-vector varies as functions of azimuthal angle from 0° to 360° and polar angle from 0° to 180°. Note that the polar angle of the incident electron will be refracted to a larger value due to the inner potential of the silicon crystal.

Figure 3 illustrates how to create a 2D **k**-space projection plot from a 3D incident electron intensity map. The upper picture shows two different **k**-vectors of incident electrons impinging on a particular absorber on/at the surface. The electron gun is assumed to be controlled to cover polar angles from 0° to 90° and azimuthal angles from 0° to 360°. All **k**-vectors of each plot have a fixed magnitude. The picture in frame 1 shows two **k**-vectors that terminate on the bottom hemisphere. Dashed lines determine the projection point of each vector on the plot. The picture in frame 2 represents the incident electron intensity at the absorber as a function of **k**-vector projection. Two points correspond to the projection of either the $\mathbf{k}_1$ or $\mathbf{k}_2$ vector. The black, gray and light gray (deep blue, yellow and light blue online) represent the intensity where black (deep blue) represents the highest, gray (yellow) the intermediate and light gray (light blue) the weakest intensities in arbitrary units.

Figure 4 shows the calculated incident electron intensity at an absorber as a function of incident electron **k**-vector on the Si(111)-(1 × 1):Cl surface by using 2D plots such as those shown in figure 3. The absorber site has been chosen as a Si atom directly bonded to a Cl adsorbate or a Cl atom itself. Because the threshold energy for the desorption of Cl^+ yield is 17 ± 0.5 eV, [9–11, 14, 32] incident electron energies (E_i) of 20, 30, or 40 eV have been used for calculation. All plots show the three-fold symmetry present on the Si(111) surface and characteristic peak points exist along with a low intensity background. For $E_i = 20$ eV, 6 high peak points can be seen in both Si and Cl absorber plots. The intensity plot for the Si absorber shows a more concentrated structure near the center than that of the Cl absorber. The plots for $E_i = 30$ eV maintain this tendency; i.e. highest points for the Si absorber are at the center whereas peak points in the Cl absorber are located near the edge. For $E_i = 40$ eV, changes from this tendency occur for both plots. These results indicate that the calculations for $E_i \leqslant \sim 30$ eV are good candidates for qualitative analysis of initial state effects in the ESD of Cl^+ from the Si(111)-(1 × 1):Cl surface.

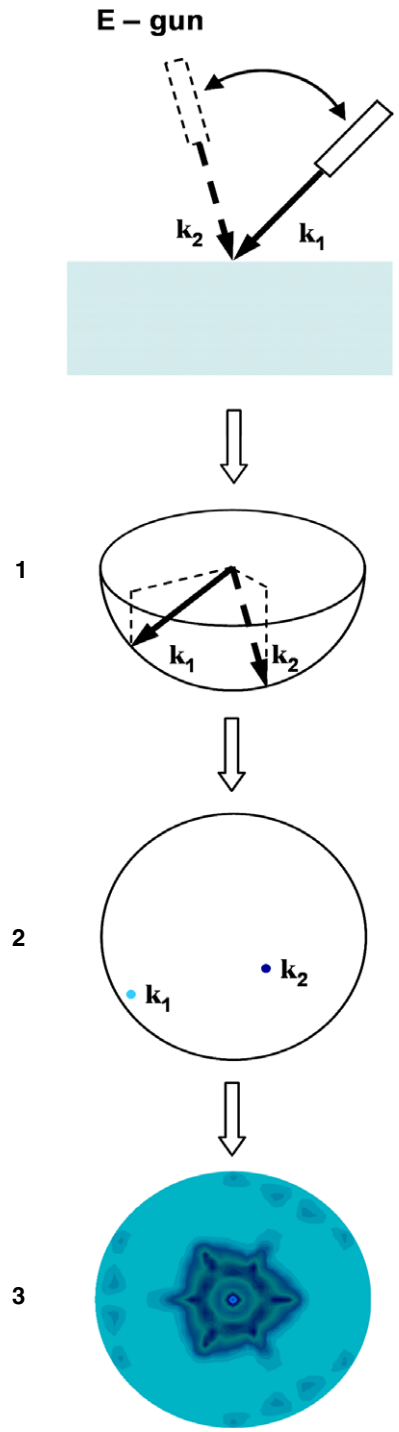

Figure 3. Illustration of the incident electron intensity plot at an absorber as a function of incident electron **k**-vector projection. The upper picture shows two **k**-vectors of the electrons incident on a surface. The electron gun is assumed to be controlled to cover polar angles from 90° to 180° and azimuthal angles from 0° to 360°. All **k**-vectors of each plot have a fixed magnitude. The picture in frame 1 shows two **k**-vectors that terminate on the bottom hemisphere. Dashed lines determine the projection point of each vector on the plot. The picture in frame 2 represents the incident electron intensity at the absorber as a function of **k**-vector projection. Two points correspond to the projection of either the $\mathbf{k}_1$ or $\mathbf{k}_2$ vector. The black, gray and light gray (deep blue, yellow and light blue) represent the intensity where black (deep blue) represents the highest, gray (yellow) the intermediate and light gray (light blue) the weakest intensity.

4. Experimental approach and sample preparation

In an effort to experimentally demonstrate DESD and to illustrate the role DESD can play in determining which sites are ESD active, we have examined the yield of Cl^+ from the Si(111)-(1 × 1):Cl, Si(7 × 7)A:Cl and Si(7 × 7)B:Cl surfaces as a function of azimuthal angle and incident electron energy. Although the apparatus and approach have been described in detail elsewhere [14], we briefly describe the most relevant aspects. For preparation of the Si(111):Cl sample, n-type Si(111) substrates were cleaned *in situ* by heating to 1300 °C for 10 s to desorb the oxide layer. These samples were cooled to 450 °C and exposed to 1×10^{-7} Torr of Cl_2 for 1000 s. These preparation conditions are known to yield a well-ordered (1 × 1) surface terminated by one monolayer (1 ML) of Cl atoms [33]. The Si(111)-(7 × 7)A:Cl structure is the usual dimer-adatom-stacking fault reconstruction with adatom and rest atom dangling bonds saturated by Cl [33, 34], and was produced by exposing the clean (7 × 7) surface to 100 L of Cl_2 at room temperature. The Si(111)-(7 × 7)B:Cl surfaces was prepared by annealing the (7 × 7)A surface for 5 min at 300 °C. Scanning tunneling microscopy (STM) studies have shown that this surface retains the stacking fault, but adatoms have been removed and the remaining rest atom dangling bonds are Cl terminated [34].

The measurements were carried out in an ultrahigh vacuum system (base pressure 2×10^{-10} Torr) equipped with a rotating sample mount, a pulsed low-energy (5–100 eV) electron gun (pulse width ∼1 μs), and a time-of-flight (TOF) mass spectrometer with unit mass resolution. The sample was mounted such that the parallel component of the electron **k**-vector pointed in the substrate $[\bar{1}\bar{1}2]$ direction (a mirror plane) at azimuth $\phi = 0°$. The electron gun has a fixed 45° polar angle of incidence relative to the sample normal. Data were acquired by leaving the electron gun and TOF spectrometer fixed, while the sample was rotated in azimuth. To ensure total ion collection, an extraction field pulse of −125 V was applied between the sample and the TOF entrance grid immediately following the electron pulse. This yielded a very reproducible TOF spectrum (not shown) that consisted solely of the $^{37}Cl^+$; $^{35}Cl^+$ isotope pair. These results indicated that the samples were clean and free from organics, hydrogen or high mass Cl containing contaminants and that no $SiCl_x$ fragments were produced.

5. Desorption mechanisms

5.1. DESD in the Si(111)-(1 × 1):Cl system

Figure 5 shows the variation of the Cl^+ yield from Si(111):Cl using 20, 30, and 40 eV incident electron energies as a function of the azimuthal angle. All the data are represented as a χ-function that is obtained by removing a smooth background curve due to incoherent secondary scattering events and is simply $I/I_0 - 1$, where I_0 is symmetry-averaged Cl^+ yield that corresponds to the ion yield without any electron diffraction effects [13]. Peaks in each data set correspond to areas of constructive electron interference at the site of the absorber atom(s), and troughs to destructive interference. The dotted

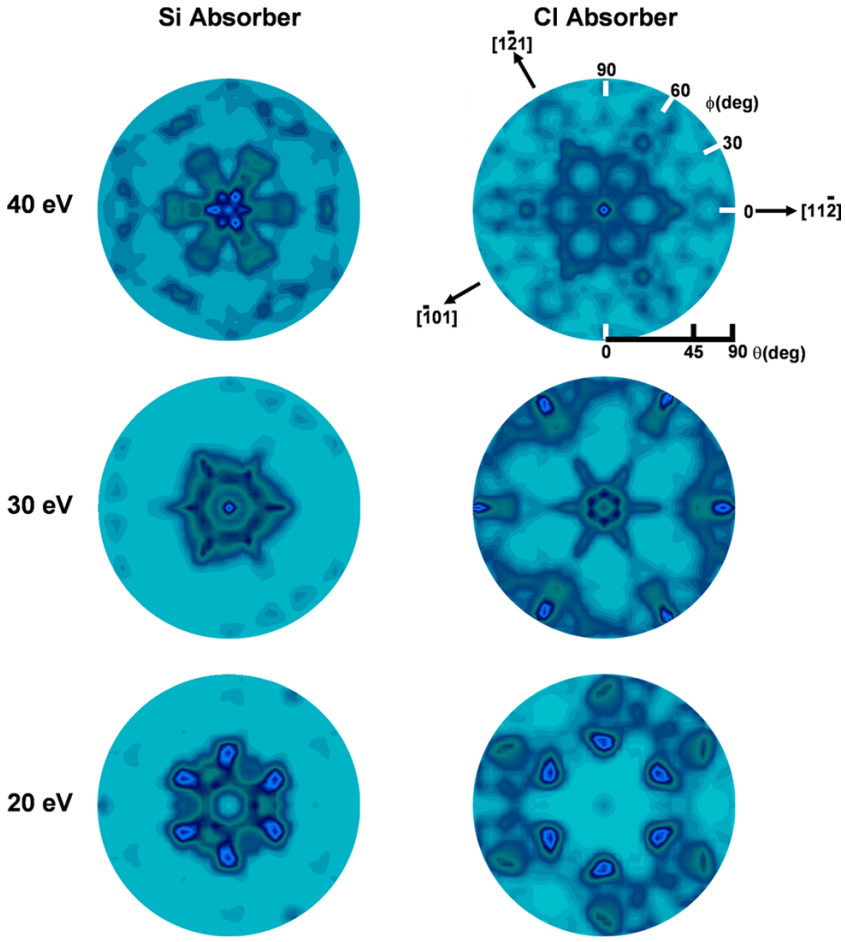

Figure 4. Calculated incident electron intensity at an absorber of the Si(111)-(1 × 1):Cl surface as a function of the incident electron **k**-vector projection. The way to derive these plots is explained in figure 3. The angles ϕ and θ represent the azimuthal and polar angles, respectively. All calculations are done at 300 K. The absorber site has been chosen as the Si atom directly bonded to the Cl adsorbate or the Cl atom itself. The plots using the Si absorber are displayed on the left side whereas the plots using the Cl absorber are displayed on the right side. Incident electron energies of 20, 30, or 40 eV were used for the calculations. The intrinsic three-fold symmetry present on the Si surface can be observed in all plots.

lines represent the theoretical calculation of incident electron intensity at the absorber. These calculations are part of the plots in figure 4 with a fixed polar angle of 45°. Calculations in the left plots use Si as the absorber and those in the right use Cl as the absorber. For comparison, χ-functions are scaled to match the calculations. For plots using $E_i = 20$ eV, the calculation with the Si absorber matches the χ-function better than that with the Cl absorber. While the Cl absorber calculation shows two additional peaks near 60°, the Si one does not show any substantial features around 60° and again it matches with the data well. Also, the phases at 0° and 120° in the Cl absorber plot are reversed. In the 30 eV plots, peaks at 30° and 90° match the data for the Si absorber well. However, they are not observed in the calculation using the Cl absorber. Even the data for $E_i = 40$ eV plots shows better agreement with calculations using the Si absorber rather than the Cl absorber. The result of this qualitative analysis shows that excitation of the Si substrates, particularly sites bound to the Cl adsorbates, are relevant to the ESD of Cl^+ from the Si(111)-(1 × 1):Cl surface.

In view of the DESD results, the threshold energy of 17 eV and the available information on the surface electronic structure [35–40] we have proposed two mechanisms for the ESD of Cl^+ from Si(111) surfaces [13, 14, 41]. The first is based on the initial ionization of the Si 3s level. The hole in the Si 3s level can be filled via Auger cascading primarily from the σ-bonding surface state [41]. The 5 eV of energy gained in the cascade event is approximately enough to excite an electron from the surface π-levels to the bottom of the lowest conduction band edge. This shallow core hole can be dressed with an exciton and as such is formally a 2-hole, 1-electron final state. Ion desorption can occur due to the hole–hole Coulomb repulsion. The second mechanism is based on direct ionization of the σ-bonding surface state. This could lead to removal of Cl^+ providing there is an excess of at least 4 eV, the energy necessary to break the Si–Cl bond. Since the σ-bonding surface state partially overlaps the P_z orbital of Si, this mechanism would be consistent with the DESD calculation. Although previous photon-stimulated desorption (PSD) studies suggested direct excitation of the Cl 3s level into valence antibonding states [10], the DESD data does not support this assignment.

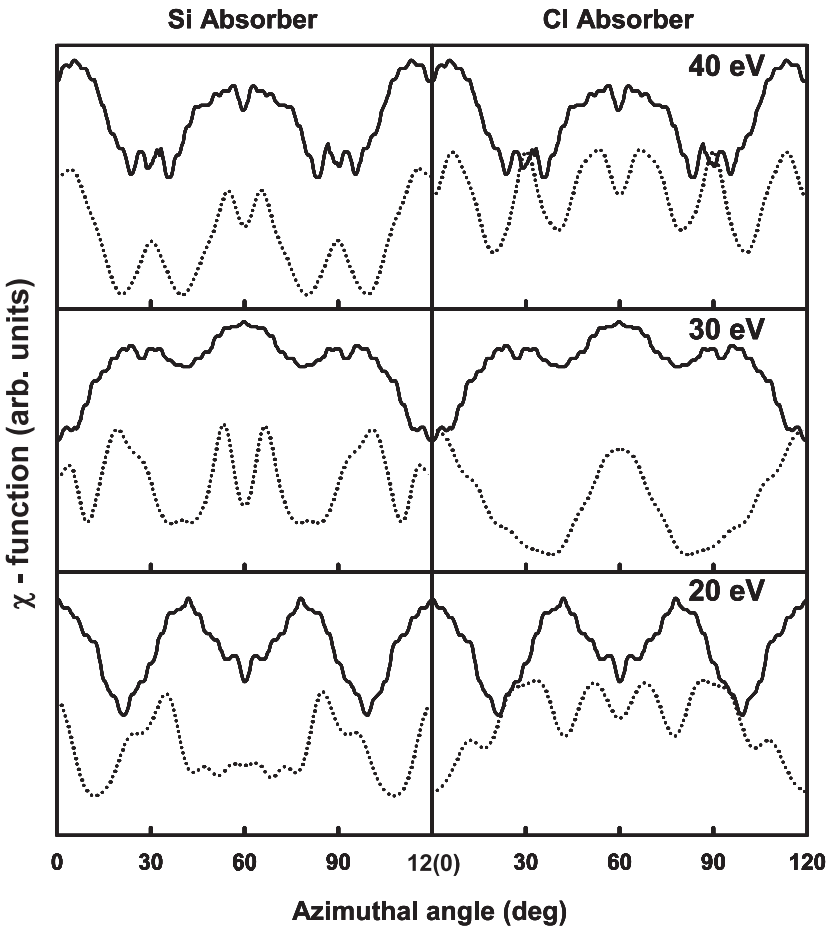

Figure 5. Qualitative comparison between experimental results of Cl^+ yield and calculations of incident electron intensity. Solid lines represent the experimental data that are the variation of the Cl^+ yield from the Si(111)-(1 × 1):Cl surface at the incident electron energy of 20, 30, or 40 eV as a function of the azimuthal angle from 0° to 120°. They are represented as a χ-function that is obtained by removing a smooth background curve due to incoherent secondary scattering events and is simply $I/I_0 - 1$ where I_0 is the symmetry-averaged Cl^+ yield that corresponds to the ion yield without any electron diffraction effect. The dotted lines represent the theoretical calculation of the incident electron intensity at the absorber. These calculations are part of the plots in figure 4 with a fixed polar angle of 45°. The Si absorber is shown on the left and the Cl absorber on the right. For the comparison, χ-functions are scaled to match the calculations. Calculations with the Si absorber show better agreement with the data for all electron energies.

5.2. Temperature effects in DESD

The width of the experimental and theoretical peaks differ. To address temperature affects, Debye–Waller factors were included in each scattering path. The one-dimensional mean square displacement is then calculated using the high-temperature limit of the Debye model, which is selected to be 450 K for Si(111) [42].

To demonstrate the importance of temperature, we examine the Cl^+ DESD data obtained using $E_i = 30$ eV at 300 and 90 K. This is shown in figure 6 where the upper two plots represent the χ-functions of the experimental Cl^+ yield from Si(111)-(1 × 1):Cl surface at 300 and 90 K, respectively. The bottom plot represents the calculation of incident electron intensity with $E_i = 30$ eV at 90 K. Comparison between the χ-functions with 90 and 300 K shows the tendency of peak sharpening as the temperature decreases. Valleys at 40° and 80° become obvious in the 90 K data compared to those in the 300 K data. Also, the peak at 60° at 300 K tends to be resolved into two peaks at 90 K. Although we cannot get a perfect match between the experimental result and the calculation, the general tendency and agreement is good.

5.3. DESD on Cl terminated Si(111)-(7 × 7):A and B surfaces: faulted versus unfaulted zones

The DESD calculation provides the sum of all partial waves from all scattering centers and our analysis has been based on matching of the χ-function of Cl^+ desorption with this summation. In order to examine whether DESD can reveal zone and site specificity, we analyzed the Cl^+ desorption based on the electron intensity distribution associated with the well known faulted and unfaulted regions of the Si(111)-(7 × 7) unit cell. These unit cells are shown in figure 7. Calculations of incident electron intensities have been done for all 42 Si rest atoms in addition to one corner hole within one unit cell or Cl bonded to these rest atoms. The calculated electron intensity in the upper left-side frame A of figure 8 is the summation for all Si sites bonded to Cl absorbates on the faulted subunit of the Si(111)-(7 × 7)A:Cl surface whereas the middle left-

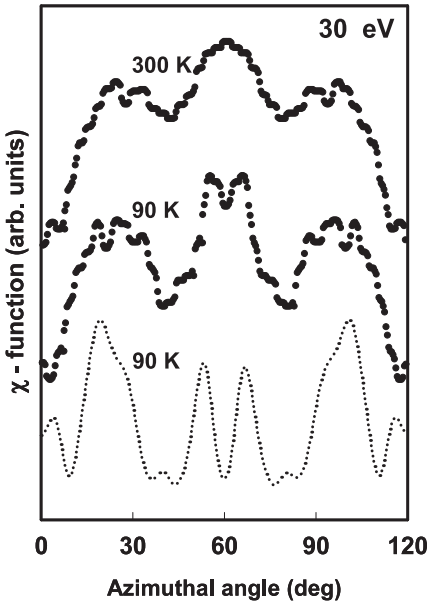

Figure 6. The Cl^+ yield at 90 and 300 K and the calculated incident electron density at the Si absorber as a function of azimuthal angle. The upper two plots represent the χ-functions of the experimental Cl^+ yield from Si(111)-(1 × 1):Cl surface with a 30 eV incident electron energy. The bottom plot represents the calculation of incident electron intensity with a 30 eV incident electron energy at 90 K. Comparison between the χ-functions with 90 and 300 K shows the tendency of peak broadening as temperature increases or peak narrowing as temperature decreases. The χ-functions have been scaled for the comparison with the calculation.

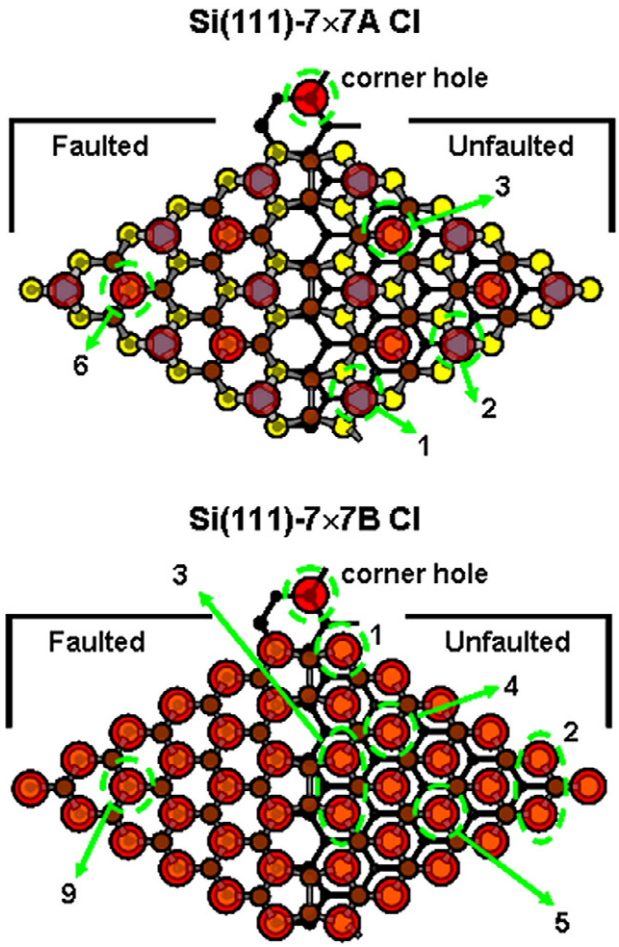

Figure 7. The several classes of termination sites within the faulted and unfaulted used in the calculation demonstrating zone specific desorption. The sites are labeled as numbered in top views of the Si(111)-(7 × 7)A:Cl and Si(111)-(7 × 7)B:Cl surface geometries. Each site class is three-fold symmetric and a single site has been identified for clarity.

side frame B is the summation for the unfaulted subunit. The correlation with the data (solid line) is clearly much closer when comparing to the unfaulted region. However, there are still some mismatches. In order to understand this, we carried out calculations that include a subset of sites where Si rest atoms are directly bonded to Cl absorbates. These sites are designated in figure 7 as class 3, 6, and corner sites. The contribution of these sites have been summed with weighting factors of 0.4, 0.2, and 0.4 and yield a close match to the data shown in the left-side frame C of figure 8. A similar analysis has been applied to the Si(111)-(7 × 7)B:Cl surface. Again, as shown in the right-side frame B, the calculated electron intensity for all Si localized sites on the unfaulted subunit matches the χ-function. However, there are still some mismatches in the relative peak heights. To address this, only sites within classes 1, 4 and 5, which are located at the edges and central part of the unfaulted region (see figure 7), have been summed with an equal weighting. A near perfect match is obtained when allowing a minor contribution from the corner hole and some weak intensity from site 9 in the faulted region. This can be seen in the right-side frame C of figure 8. Thus, there appears to be clear site specificity and a propensity for removal of Cl^+ from the unfaulted subunit versus other regions.

Assuming that the initial and final states are similar to those active in the ESD of Cl^+ from Si(111)-(1 × 1):Cl, this interesting zone specificity phenomenon can be related to lifetime effects resulting from the increased strain in the faulted region and the reduced density of states at the Fermi level in the unfaulted region. The strain causes the surface layer in the faulted region to buckle giving rise to Si atoms that are higher than those in the unfaulted zone by 0.2 Å [34]. In the elevated faulted region, surface electronic states localized on the Si–Si back bond are slightly decoupled from bulk electronic states of the Si bond. Thus, the bandwidth of surface electronic states containing significant Si character will be narrowed. It is known that the desorption probabilities of adsorbates induced from localized holes are associated with hole–hole correlation energies (U_h) and bandwidths (ΔE) [43]. When the bandwidth is small compared to the repulsion energy, increased hole localization can occur. In this case, localized holes at Si–Si back bonds likely induce Si–Si bond breakage but do not induce desorption of Cl^+ or any other cationic products. In addition, three bonds between Si adatoms and Si restatoms in the Si(111)-(7 × 7)A:Cl surface are distorted so increased hole–hole localization at those sites can also increase back-bond breakage while inhibiting Cl^+ desorption. Similar hole localization arguments have been given to explain the laser-induced desorption of adatoms from Si(111)-(7 × 7) [44].

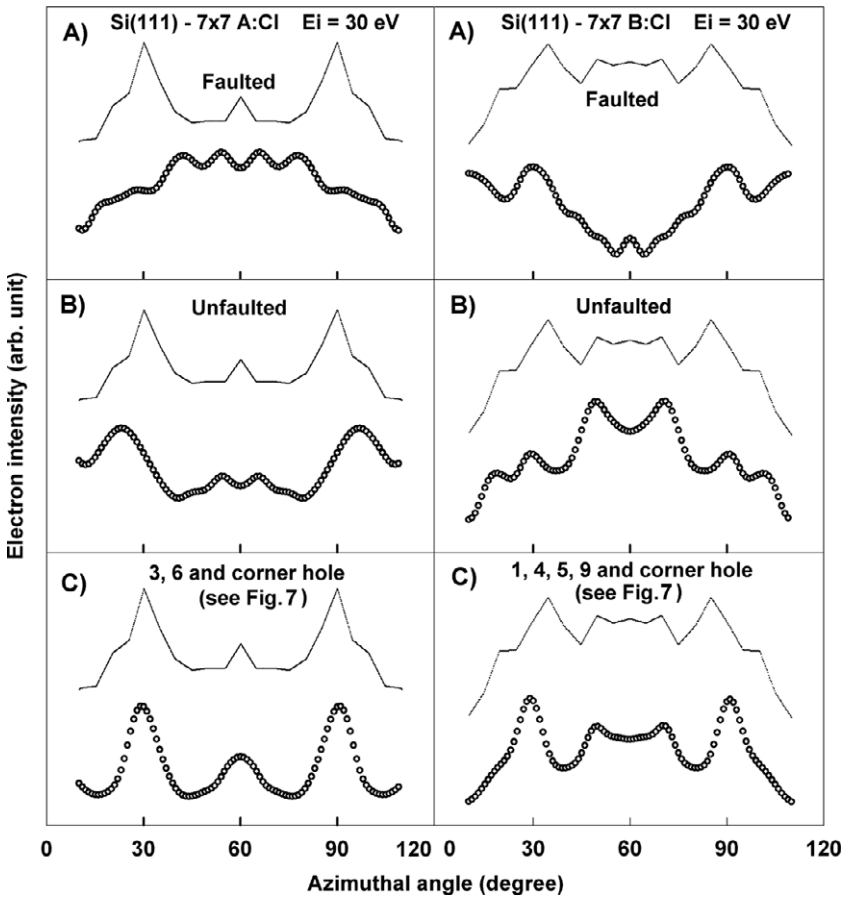

Figure 8. A comparison of DESD from faulted and unfaulted regions of Si(111)-(7 × 7)A:Cl and Si(111)-(7 × 7)B:Cl surfaces. The amplitudes in the calculations (dotted line) are scaled to match the χ-functions (solid line). Frame A is the comparison to the summation of all localized Si sites on the faulted subunit and frame B, the unfaulted subunit. In the left side of frame C, only classes 3, 6, and a corner hole (shown in figure 7) with the weighting factors of 0.4, 0.2, and 0.4 have been summed. In the right side of frame C, only classes 1, 4, 5, 9 and a corner hole (shown in figure 7) have been summed with the weighting factors of 0.23, 0.23,, 0.23, 0.23, and 0.08, respectively.

Previous studies of electron-stimulated desorption from surfaces containing electronegative adsorbates demonstrated large yield increases due to enhanced lifetimes brought about by reduced screening [1]. This resulted from a reduction of the density of states at the Fermi level. Since calculations and STM measurements indicate a reduced density of states at the Fermi level in the unfaulted zones of Si(111)-(7 × 7) [45], screening in this zone will be reduced. Thus, holes in Si–Cl σ-bonding surface states have longer lifetimes so precisely the same effect observed previously can lead to selective removal of Cl^+ from the unfaulted regions.

6. Conclusions

A theoretical description and experimental demonstration of diffraction in electron-stimulated desorption (DESD) has been presented. Specifically, initial state effects in DESD of Cl^+ from Si(111)-(1 × 1):Cl, Si(111)-(7 × 7)A:Cl and Si(111)-(7 × 7)B:Cl surfaces is examined and a theoretical treatment that includes spherical-wave effects and multiple scattering of low-energy incident electron is developed. Qualitative comparison of the experimental data with theory and analysis of the yields versus incident electron energy indicate that Cl^+ desorption from Si(111)-(1×1):Cl and Si(111)-(7×7):Cl surfaces initially involves states with significant Si 3s, Cl 3s and/or Si–Cl σ-bonding character. Holes in any of these three levels can be dressed with an electron–hole pair giving rise to repulsive two-hole, one–electron final states. We have also demonstrated that DESD can reveal zone and site specific information in the stimulated desorption of cations. Specifically, in the Si(111)-(7 × 7):Cl case, there is a propensity for Cl^+ desorption from the unfaulted versus faulted zones of the 7×7 reconstructed rest atom area. In addition, this propensity seems to be primarily related to specific sites within the unfaulted zone. The spatial selectivity may be related to (i) increased hole localization in the Si–Si backbond within the faulted region, (ii) more rapid hole-hopping to faulted zone center sites and (iii) reduced screening within the unfaulted region.

DESD is expected to be a general phenomenon, especially when dealing with surfaces and adsorbates with strongly screened and localized excitations. It may be useful as a pre-patterning strategy for semiconductor and metal-oxide surfaces at the nanoscale. Since the ability to spatially control the production of defects and removal of adsorbates is very important with respect to developing scalable approaches to nanopatterning, we are currently examining whether DESD

persists in the lower-energy channels which are dominated by neutral desorption.

Acknowledgments

The initial experimental and theoretical work was supported by the United States Department of Energy, Office of Science, Contract DE-FG02-02ER15337. The writing of this manuscript was supported by the United States National Science Foundation, Nanoscience Interdisciplinary Research Team (NIRT) Grant No. 0403671. The authors thank Dr Greg K Schenter for very useful conversations and assistance during the initial phases of this program.

References

[1] Orlando T M, Burns A R, Jennison D R and Stechel E B 1992 *Phys. Rev.* B **45** 8679
[2] Alexandrov A, Piacentini M, Zema N, Felici A C and Orlando T M 2001 *Phys. Rev. Lett.* **86** 536
[3] Menzel D and Gomer R 1964 *J. Chem. Phys.* **41** 3311
[4] Menzel D and Gomer R 1964 *J. Chem. Phys.* **40** 1164
[5] Knotek M L and Feibelman P J 1978 *Phys. Rev. Lett.* **40** 964
[6] Ramsier R D and Yates J T 1991 *Surf. Sci. Rep.* **12** 243
[7] Czyzewski J J, Madey T E and Yates J T Jr 1974 *Phys. Rev. Lett.* **32** 777
[8] Cheng C C, Gao Q, Choyke W J and Yates J T Jr 1992 *Phys. Rev.* B **46** 12810
[9] Yonezawa T, Daimon H, Nakatsuji K, Sakamoto K and Suga S 1994 *Appl. Surf. Sci.* **79/80** 95
[10] Durbin T D, Simpson W C, Chakarian V, Shuh D K, Varekamp P R, Lo C W and Yarmoff J A 1994 *Surf. Sci.* **316** 257
[11] Guo Q, Sterratt D and Williams E M 1995 *J. Electron Spectrosc. Relat. Phenom.* **72** 31
[12] Guo Q, Sterratt D and Williams E M 1996 *Surf. Sci.* **356** 75
[13] Sieger M T, Schenter G K and Orlando T M 1999 *Phys. Rev. Lett.* **82** 3348
Sieger M T and Orlando T M 2000 *Surf. Sci.* **451** 31
[14] Oh D, Sieger M T and Orlando T M 2006 *Surf. Sci.* **600** L245
[15] Flege J I, Schmidt T, Falta J and Materlik G 2002 *Surf. Sci.* **507–510** 381
[16] Falta J, Hille A, Schmidt T and Materlik G 1999 *Surf. Sci.* **436** L677
[17] Flege J I, Schmidt T, Bätjer J, Cakmak M, Materlik G and Falta J 2005 *New J. Phys.* **7** 208
[18] Duke C B and Laramore G E 1970 *Phys. Rev.* B **2** 4765
Laramore G E and Duke C B 1970 *Phys. Rev.* B **2** 4783
[19] Rehr J J and Albers R C 1990 *Phys. Rev.* B **41** 8139
[20] Trehan R and Fadley C S 1986 *Phys. Rev.* B **34** 6784
[21] Burns A R, Stechel E B and Jennison D R 1987 *Phys. Rev. Lett.* **58** 250
[22] Burns A R, Jennison D R and Stechel E B 1994 *Phys. Rev. Lett.* **72** 3895
[23] Stechel E B, Burns A R and Jennison D R 1995 *Surf. Sci.* **340** 71
[24] Berakdar J and Das M P 1997 *Phys. Rev.* A **56** 1403
[25] Feder R, Gollisch H, Meinert D, Scheunemann T, Artamonov O M, Samarin S N and Kirschner J 1998 *Phys. Rev.* B **58** 16418
[26] Kheifets A S, Iacobucci S, Ruocco A, Camilloni R and Stefani G 1998 *Phys. Rev.* B **57** 7360
[27] Kaduwela A P, Friedman D J and Fadley C S 1991 *J. Electron Spectrosc. Relat. Phenom.* **57** 223
[28] Zabinsky S I, Rehr J J, Aukudinov A, Albers R C and Eller M J 1995 *Phys. Rev.* B **52** 2995
[29] Ankudinov S I, Zabinsky S I and Rehr J J 1996 *Comput. Phys. Commun.* **98** 359
[30] Watson P R, Van Hove M A and Hermann K 2001 *NIST Surface Structure Database—Ver. 4.0* (Gaithersburg, MD: National Institute of Standards and Technology)
[31] Citrin P H, Rowe J E and Eisenberger P 1983 *Phys. Rev.* B **28** 2299
[32] Nakatsuji K, Matsuda K, Yonezawa T, Daimon H and Suga S 1996 *Surf. Sci.* **363** 321
[33] Boland J J and Villarrubia J S 1990 *Phys. Rev.* B **41** 9865
[34] Villarrubia J S and Boland J J 1989 *Phys. Rev. Lett.* **63** 306
[35] Martin-Gago J A, Roman E, Refolio M C, Lopez-Sancho J M, Rubio J, Hellner L and Comtet G 1999 *Surf. Sci.* **424** 82
[36] Schnell R D, Rieger D, Bogen A, Himpsel F J, Wandelt K and Steinmann W 1985 *Phys. Rev.* B **32** 8057
[37] Johansson L S O, Uhrberg R I G, Lindsay R, Wincott P L and Thornton G 1990 *Phys. Rev.* B **42** 9534
[38] Mednick K and Lin C C 1978 *Phys. Rev.* B **17** 4807
[39] Schlüter M and Cohen M L 1978 *Phys. Rev.* B **17** 716
[40] Pandey K C, Sakurai T and Hagstrum H D 1977 *Phys. Rev.* B **16** 3648
[41] Orlando T M, Oh D, Sieger M T and Lane C D 2004 *Phys. Scr.* T **110** 256
[42] Hobler G, Simionescu A, Palmetshofer L, Jahnel F, von Criegern R, Tian C and Stingeder G 1996 *J. Vac. Sci. Technol.* B **14** 272
[43] Ramaker D E 1983 *J. Vac. Sci. Technol.* A **1** 1137
[44] Kanasaki J, Ishida T, Ishikawa K and Tanimura K 1998 *Phys. Rev. Lett.* **80** 4080
[45] Brommer K D, Galvan M, Dal Pino A Jr and Joannopoulos J D 1994 *Surf. Sci.* **314** 57